# Aqueous Self-Assembly within the Homologous Peptide Series A$_n$K

Çelen Çağrı Cenker,[†] Seyda Bucak,[‡] and Ulf Olsson*,[†]

[†]Division of Physical Chemistry, Chemistry Department, Lund University, Box 124, SE-22100 Lund, Sweden
[‡]Department of Chemical Engineering, Yeditepe University, 34755 Istanbul, Turkey

ABSTRACT: We compare the aqueous self-assembly behavior within the homologous peptide series A$_n$K, where A is alanine, K is lysine, and n = 4, 6, 8, and 10. The aqueous peptide solubility, ϕ_s (volume fraction), depends strongly on the number of hydrophobic alanine residues and decreases approximately as $\phi_s \approx 10^{-n}$. Also the self-assembly structure depends on n. A$_4$K is highly water-soluble and shows no relevant self-assembly. A$_6$K, which has been extensively studied previously, forms hollow nanotubes in water. A$_8$K and A$_{10}$K self-assembly is characterized here using a combination of small- and wide-angle X-ray scattering, static and dynamic light scattering, cryo transmission electron microscopy, and circular dichroism spectroscopy. They both form similar thin rodlike aggregates with lengths on the order of 100 nm and a biaxial cross-section with dimensions of 4 nm × 8 nm. We show that different sample preparation protocols result in different lengths of the A$_{10}$K rodlike aggregates. On the basis of these findings, the question of thermodynamic equilibrium of peptide self-assembly is discussed.
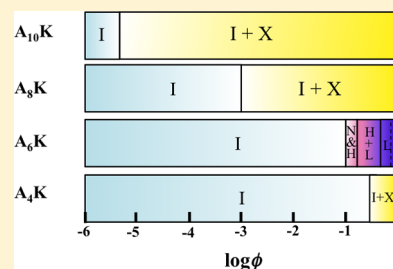
1. INTRODUCTION

Peptide self-assembly has received considerable attention in recent years.[1−4] The reasons are essentially three-fold. First, peptide fibrillation and amyloid formation appear to be associated with a large number of neurodegenerating diseases.[5] Second, there are many peptide-based materials with potential applications in nanotechnology and medical technology.[6−8] Third, the number of peptide-based drugs on the market is rapidly growing,[9] and for the formulation of such drugs at higher concentrations, aggregation can be an issue.

Thanks to the advancements in solid-state synthesis,[10,11] custom-designed synthetic peptides are readily obtained, allowing for systematic studies of peptide−peptide interactions and materials design. Typically, aggregation is driven by hydrophobic interactions, while directional hydrogen bonding influences the local molecular packing in the aggregates, often with extended β-sheets. Electrostatic and steric excluded volume interactions may also influence the peptide−peptide interactions and the molecular packing in the aggregates. A net peptide charge generally provides colloidal stability of the peptide aggregates.

We have recently characterized the self-assembly of the synthetic designed peptide A$_6$K (A = alanine and K = lysine) in aqueous solution.[12−15] This peptide shows a spectacular aggregation into hollow nanotubes of 26 nm radius, above a critical concentration, followed by a transition to a smectic lamellar phase as the peptide concentration is increased. In this paper we extend our study on the aggregation of model peptides to consider the homologous series A$_n$K, where n = 4, 6, 8, and 10 is the number of alanine residues in the peptide chain. As the alanine side chain is uncharged and hydrophobic, the peptide becomes increasingly hydrophobic with increasing n.

The peptides studied here are uncapped. Similar A$_n$K peptides were studied in the pioneering work of Zhang et al.[16,17] and later by Zhao et al.[18,19] However, in these cases the peptides were capped, either at both ends or at the N-terminus. However, aggregation behavior observed for the capped peptides is different from the behavior observed here. For example, capped A$_6$K forms fibrils,[18] while uncapped A$_6$K forms nanotubes.[12,13]

In what follows, we will demonstrate how the aqueous solubility and self-assembly behavior vary when the number of alanine residues changes in the A$_n$K model peptide. Furthermore, we address the issue of thermodynamic stability of the peptide self-assembly. This is very important for the understanding and the applications of these materials. However, in the huge literature on peptide self-assembly, it is seldom clear whether the observed aggregates represent an equilibrium state, characterized, e.g., by an equilibrium size distribution, or correspond to a precipitated peptide phase and hence a two-phase equilibrium.

2. MATERIALS AND METHODS

2.1. Materials. The trifluoroacetate (tfa) salts of A$_n$K peptides with n = 4, 6, 8, and 10 were purchased from CPC Scientific, Inc. with purities of 95.6%, 97.8%, 97.4%, and 96.2%, respectively, and they were used without further purification. Heavy water, D$_2$O (99.8%), was obtained from Armar Chemicals. Samples were studied in D$_2$O rather than in H$_2$O due to planned NMR experiments. The peptide concentration here is given as a volume fraction, ϕ. The densities that were used to convert from weight fraction to ϕ are 1.44, 1.45, 1.50, and 1.26 g/cm^3 for n = 4, 6, 8, and 10, respectively, while the D$_2$O

density is 1.11 g/cm³. The peptide densities were measured using an Anton Paar DMA 5000 densitometer.

Samples were prepared by weighing the components, freeze-dried peptide and heavy water, in glass vials that where sealed by a plastic cap and left to equilibrate at room temperature (ca. 22 °C). For individual samples, typically 0.5−1 g was prepared. In certain cases a dilution series was prepared from a larger stock solution.

2.2. Methods. Small-angle X-ray scattering (SAXS) experiments were conducted on beamline I711 at the MAX II storage ring in Lund, Sweden.[20] A monochromatic beam of point collimation with a wavelength λ = 1.1 Å was used. The sample-to-detector distance was 1.2 m. The scattered intensity was recorded with a 2D position-sensitive charge-coupled device (CCD) detector (165 mm diameter in active area 1024 pixels × 1024 pixels from Marresearch, Gmbh) as a function of the scattering vector, $q = (4\pi/\lambda) \sin(\theta/2)$, where θ is the scattering angle. The data were then radially averaged using the FIT2D program and normalized with the primary beam intensity.

The samples were measured in high-quality quartz capillaries. For the analysis of the scattering patterns, the detector response was normalized with respect to the incoming beam intensity and exposure time. The scattering of the solvent and the capillary were subtracted from the sample scattering.

The wide-angle X-ray scattering (WAXS) measurements were performed on the laboratory-based SAXS instrument Ganesha from JJXray. The instrument has a Pilatus 300K detector and a Genix 3D X-ray source. λ = 1.54 Å, and the sample-to-detector distance was 180 mm.

Cryo transmission electron microscopy (cryo-TEM) images were recorded at the National Center for High Resolution Electron Microscopy within the Chemistry Department at Lund University. To improve the wetting properties, the grids were glow-discharged, which temporarily forces the hydrophobic surface of the carbon grid to become more hydrophilic. After glow discharging, the sample was carefully placed on the grid with a micropipet in a closed controlled environment system (CEVS) to ensure stable temperature conditions and to minimize loss of solvent during sample preparation.[21] The samples were blotted with filter paper to create a thin film on the grid and then plunged in liquid ethane and transferred to liquid nitrogen, where they were kept until the experiment. A Philips CM120 BioTWIN Cryo, equipped with a postcolumn energy filter (Gatan GIF100), with an acceleration of 120 kV, was used in our experiments.

Circular dichroism (CD) experiments were performed on a Jasco J-815 CD spectrometer equipped with a Jasco PTC-423S/15 temperature control unit. The spectra in the range of 190−260 nm were collected at a constant temperature of 20 °C with 0.01 mm thick quartz windows. The experiments were run in continuous mode with a 1 nm bandwidth, 50 nm/min scan rate, and digital integration time per data point (DIT) of 8 s. Each spectrum is the average of three scans. The water baseline was subtracted. Only data recorded with an HT voltage of less than 800 were plotted. All measurements were originally measured in millidegrees and converted to units of mean residue ellipticity.

Turbid samples were investigated with a 3D light scattering instrument from LS instruments, which employs a 3D cross-correlation technique with a modulation unit.[22,23] The instrument is equipped with a He−Ne laser light source with a wavelength of 632.8 nm and a maximum power of 35 mW. The scattered light is collected by two Avalanche photodiodes and then analyzed by a Flex correlator in a 3D cross-correlation configuration. The samples were measured in 5 mm NMR tubes, type 5TA, purchased from Armar Chemicals.

Light scattering experiments were also performed on an ALV/DLS/SLS-5022F goniometer system with an ALV-7004 correlator. The laser source here is a 22 mW He−Ne laser with a wavelength of 632.8 nm. A software-controlled attenuator optimized the laser intensity.

3. RESULTS AND DISCUSSION

3.1. Aqueous Peptide Solubility in the Homologous Series A_nK. When the aqueous peptide concentration is sufficiently low, the peptides are expected to be soluble as individual monomers in water. Molecular self-assembly into aggregates can be stepwise or, if the self-assembly is highly cooperative, can begin abruptly at a well-defined concentration. The latter is typical for the micellization of long-chain amphiphiles, and the critical concentration is referred to as the critical micellization concentration, cmc.[24] The micelles formed are equilibrium aggregates characterized by an equilibrium size distribution that typically varies with the concentration. Micellization does not involve any phase transition and occurs within an isotropic solution phase. Aggregates formed by a highly cooperative aggregation process can also be in nonequilibrium, as in the precipitation from a supersaturated solution. Here, the aggregates, if sufficiently small, are often referred to as nanoparticles. This nanoparticle formation strictly involves a phase transition with a phase boundary typically corresponding to the equilibrium solubility of monomers. Above this phase boundary the solution of monomers coexists with a denser, e.g., solid, phase in a two-phase region.

Alanine is a hydrophobic amino acid, and for the homologous series A_nK, the peptide monomer solubility is expected to decrease with increasing n. The aqueous solubility of A_6K has previously been determined to be $\phi_s = 0.1$ (volume fraction) corresponding to a molar concentration of $c_s = 0.4$ M.[12] Above this concentration, the peptides aggregate into nanotubes that in turn assemble as a nematic phase after a narrow two-phase region. It has not been firmly established whether the nanotubes form already in the isotropic phase at a critical aggregation concentration near the isotropic-to-nematic transition or if aggregation occurs first after passing the phase boundary, i.e., as a precipitation. In either case, we conclude that the monomeric solubility is $c_s = 0.4$ M.

A_4K is highly soluble in water up to a concentration of $\phi = 0.4$ ($c = 2$ M). Above this concentration the isotropic peptide solution coexists with an excess solid phase, possibly corresponding to a hydrated crystal. The isotropic peptide solution phase was investigated by SAXS in the whole concentration range and showed no sign of aggregation. Thus, we conclude that the aqueous solubility of A_4K is $c_s = 2$ M.

The aqueous solubilities of A_8K and $A_{10}K$ are significantly lower and were measured using static light scattering. Samples of different concentrations were prepared by dilution from stock solutions, $\phi = 0.030$ in the case of A_8K and $\phi = 0.035$ in the case of $A_{10}K$. The scattered intensity was measured at 90°, and the average from three consecutive measurements was taken. The results are presented in Figure 1, where the
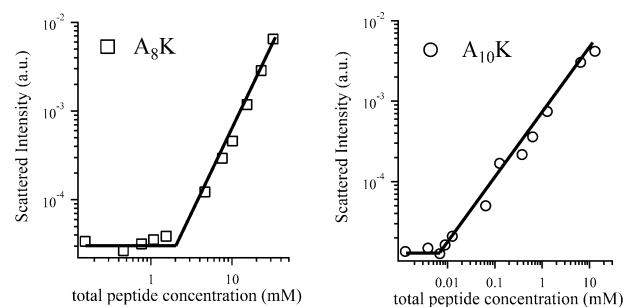

Figure 1. Variation of the scattered light intensity with the peptide concentration for A_8K (a, left) and $A_{10}K$ (b, right). Solid lines are only guides to the eye.

scattered intensity is plotted as a function of the peptide concentration. Because the large peptide aggregates scatter much more light than the monomers, the solubility is identified as the concentration below which the scattered intensity practically levels off to a constant. The solubilities were found to be $\phi_s = 7.3 \times 10^{-4}$ (2 mM) and $\phi_s = 4.7 \times 10^{-6}$ (7.4×10^{-3} mM) for A_8K and $A_{10}K$, respectively.

In Figure 2, we have plotted the aqueous solubility as a function of n, the number of alanine residues, for the four
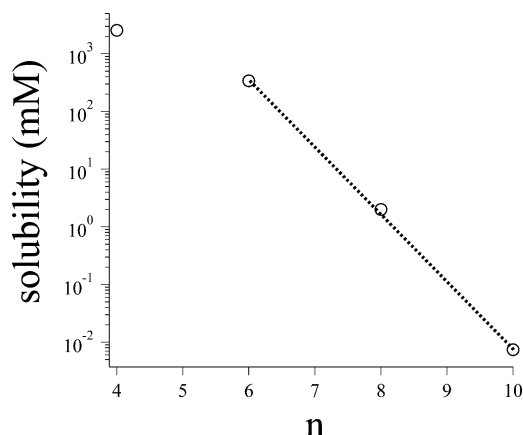

Figure 2. Aqueous solubility (mM) of A_nK as a function of the number of alanine residues, n. The solubility drops by approximately an order of magnitude per additional alanine residue.

studied A_nK peptides. As can be seen, the solubility decreases by approximately 1 order of magnitude for every additional alanine residue. This is a strong dependence similar to that observed for the homologous series of linear alkanes, alcohols, etc. where the aqueous solubility decreases by approximately 1 order of magnitude for every two methylene groups.[25] The similarity can be understood quantitatively, as every alanine residue adds a $-CHCH_3$ group, similar in size and hydrophobicity to $-CH_2CH_2-$. The other parts of the alanine residue are $-NH-$ and $-CO-$, which can hydrogen bond with water and only weakly influence the solubility.

3.2. Self-Assembly Structure of A_8K and $A_{10}K$. The shortest peptide, A_4K, did not show any sign of aggregation, using SAXS (data not shown), below the solubility limit of ca. 40 vol %. The scattered intensity showed no variation with the scattering vector, q.

The A_6K-water system has been characterized in detail.[12,13] In a concentration range of $\phi = $ ca. 0.10−015 in water, it forms hollow nanotubes with a monodisperse cross-section diameter of 52 nm and where the nanotubes are organized in a nematic phase.

Increasing the number of alanine residues to 8 or 10 results in a significantly different self-assembly structure. Figure 3 shows cryo-TEM images obtained from from A_8K at $\phi = $ 0.0074 (a, b) and from $A_{10}K$ at $\phi = $ 0.0087 (c, d). The two peptides form similar rodlike aggregates. As estimated from the images, the aggregates are on the order of 100 nm long and have a cross-section diameter of a few nanometers.

The aggregates were further characterized by SAXS. When analyzing the data, we assume that the scattered intensity, $I(q)$, can be written as a product of the particle form factor, $P(q)$, and a structure factor, $S(q)$, reporting on the interparticle interactions, i.e.[26]
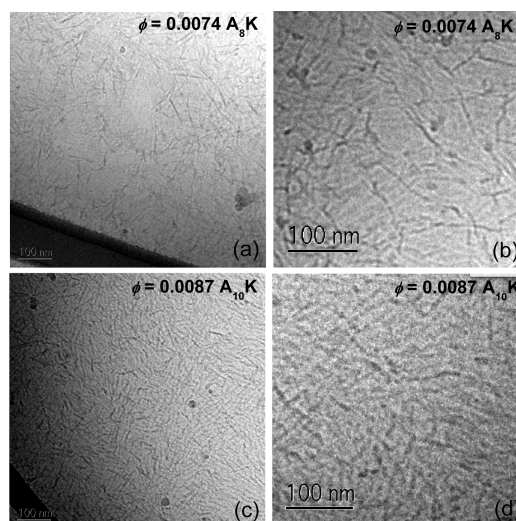

Figure 3. Cryo-TEM images for A_8K ($\phi = 0.0074$) (a, b) and for $A_{10}K$ ($\phi = 0.0087$) (c, d). Scale bars correspond to 100 nm.

$$I(q) \approx \phi P(q)\, S(q) \qquad (1)$$

where ϕ is the aggregate volume fraction. In Figure 4a we present the concentration-normalized scattering patterns, $I(q)/$
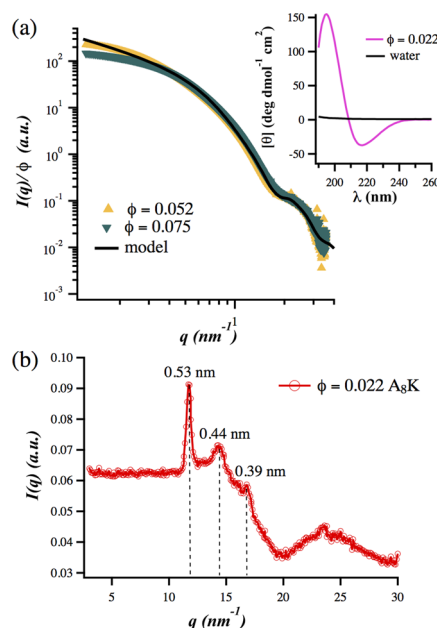

Figure 4. (a, Top) Concentration-normalized SAXS data from different A_8K concentrations. The solid line shows the form factor of long rods having an elliptical cross-section with semiaxes $a = 1.9$ nm and $b = 4.2$ nm. Inset: CD spectra obtained for $\phi = 0.022$, 0.015, and 0.0074. (b, Bottom) Background-subtracted WAXS pattern from a $\phi = 0.022$ sample of A_8K.

ϕ, obtained from two concentrations, $\phi = 0.052$ and 0.075, of A_8K. As can be seen, the normalized data overlap at higher $q > 0.4$ nm^{-1}, meaning that the aggregates have the same cross-section. The decrease of the normalized intensity at lower q values with increasing peptide concentration can be attributed to $S(q)$ and is consistent with repulsive interparticle interactions. Repulsive interactions are indeed expected, as the peptide aggregates carry a net positive charge. From the

present q range ($0.1-4$ nm^{-1}) we are unable to determine the length, L, of the rods, but we can estimate the cross-section dimensions.

We first modeled the aggregates as long cylinders with a circular cross-section, including polydispersity. A better agreement between the model and experimental data is however obtained if we allow the cross-section to be biaxial. Shown in Figure 4a, as a solid line, is the calculated scattering curve for long rods with an elliptical cross-section having semiaxes $a = 1.9$ nm and $b = 4.2$ nm. With an elliptical cross-section, the isotropically averaged form factor is given by[27]

$$P(q) = \int_0^{\pi/2} \int_0^{\pi/2} \left(\frac{2J_1(qr(a, b, \phi, \alpha))}{qr(a, b, \phi, \alpha)} \frac{\sin(qL\cos(\alpha)/2)}{qL\cos(\alpha)/2} \right)^2 d\phi \sin\alpha d\alpha \quad (2)$$

where $r(a,b,\phi,\alpha) = a^2 \sin^2\phi + b^2 \cos^2\phi$ and L is the rod length that we in the calculation allowed to be $\gg 1/q_{min} = 10$ nm. As can be seen, there is a good agreement between the model and the experimental data. As mentioned above, the deviation at lower q can be attributed to the structure factor and repulsive interactions.

As an inset in Figure 4a we show a CD spectrum obtained from $\phi = 0.022$, expressed as the molar ellipticity. As a background reference, the signal from heavy water is also shown. The spectrum shows a positive band at $\lambda = 195$ nm and a negative band at $\lambda = 215$ nm, consistent with a β-sheet peptide arrangement.

To investigate the peptide arrangement further in the aggregates, we also performed a WAXS experiment for a sample with $\phi = 0.022$. The background-subtracted WAXS pattern is presented in Figure 4b. Two clear diffraction peaks, corresponding to spacings of 5.3 and 4.4 Å are observed in addition to a weak diffraction peak corresponding to 3.9 Å. These reflections demonstrate a crystalline peptide arrangement in the aggregates. Interestingly, the same three spacings, within experimental uncertainty, were also identified in the case of A$_6$K nanotubes[14] and are similar to the first three reflections obtained from oligoalanine, e.g., A$_7$,[28] indicating a similar local packing. However, further experiments are necessary to confirm this similarity as well as the possible structural relationship to other β-sheet fibrils.[29]

As suggested by the cryo-TEM images (Figure 1), A$_{10}$K forms aggregates very similar to those of A$_8$K. This is also confirmed by SAXS. The normalized SAXS intensities, $I(q)/\phi$, obtained from five different concentrations in the range of $0.0087 \leq \phi \leq 0.133$ are presented in Figure 5a. The normalized data overlap, except at lower q, where we see the increased influence of the structure factor with increasing concentration. The data can be described with a form factor similar to that for A$_8$K. The solid line in Figure 5a corresponds to the form factor of a long rod with an elliptical cross-section having semiaxes $a = 1.9$ nm and $b = 4.8$ nm. Thus, the b-axis appears to be ca. 15% longer for A$_{10}$K compared to A$_8$K aggregates. The length of an individual A$_{10}$K peptide is ca. 20% longer than that of A$_8$K, which could be the explanation for the different b-axes if the peptides are oriented in this direction in the aggregate.

As an inset in Figure 5a we also present CD data from three different concentrations, $\phi = 0.00087$, 0.0018, and 0.0087, again expressed as the molar ellipticity. As in the case of A$_8$K, the CD spectra indicate the presence of β-sheet-type packing.

Also the WAXS pattern obtained from A$_{10}$K is very similar to that obtained from A$_8$K. The WAXS pattern from a $\phi = 0.026$ sample is presented in Figure 5b. The three main diffraction
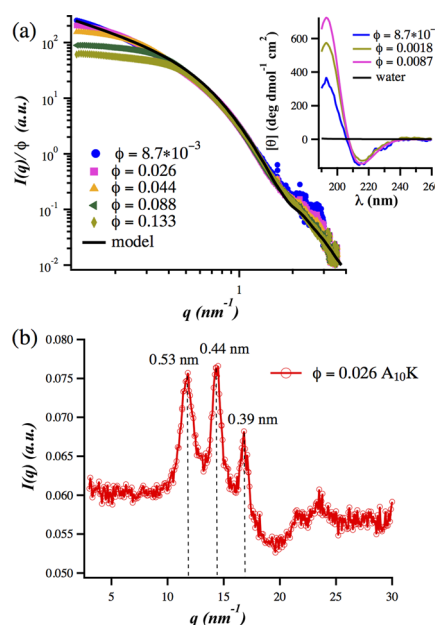

Figure 5. (a, Top) Concentration-normalized SAXS data from different A$_{10}$K concentrations. The solid line shows the form factor of long rods having an elliptical cross-section with semiaxes $a = 1.9$ nm and $b = 4.8$ nm. Inset: CD spectra obtained for $\phi = 8.7 \times 10^{-4}$, 0.0018, and 0.0087. (b, Bottom) WAXS pattern from a $\phi = 0.026$ sample of A$_{10}$K.

peaks are identical to the ones observed for A$_8$K, indicating that the peptides are arranged in similar ways in the two cases.

3.3. Dynamic Light Scattering: Measuring the Rod Lengths. To determine the lengths of the rods, dynamic light scattering (DLS) experiments were performed on A$_{10}$K samples. A series of samples, in the concentration range $0.00037 \leq \phi \leq 0.0148$, were prepared by dilution from a $\phi = 0.036$ stock solution. In Figure 6 we present the correlation
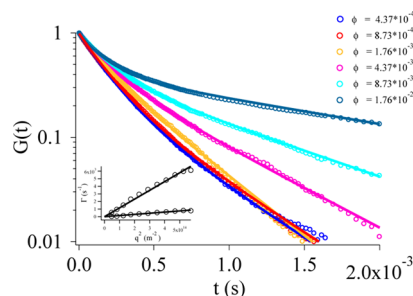

Figure 6. Normalized $G(t)$ for different ϕ values of A$_{10}$K. Γ vs q^2 for $\phi = 8.7 \times 10^{-3}$ is shown as an example in the inset.

function, $G(t)$, obtained from the different concentrations plotted on a semilogarithmic scale. $G(t)$ is given by[30]

$$G(t) = \frac{g^{(2)}(t) - 1}{\beta} = |g^{(1)}(t)|^2 \quad (3)$$

where $g^{(1)}(t)$ and $g^{(2)}(t)$ are the correlation functions of the electric field and the intensity, respectively, and β is an instrumental constant, close to unity.

As can be seen in Figure 6, the correlation functions are nonexponential (an exponential decay would have been seen as a straight line in the semilogarithmic plot). For the two lowest

concentrations, $\phi = 0.00037$ and 0.00073, the correlation functions overlap and the deviation from a single exponential decay is relatively small. The deviation, however, clearly increases with increasing concentration. While the initial, short-time, decay is essentially concentration independent, the concentration dependence lies in the long-time tail. Thus, we consider two modes: a fast concentration-independent mode and a slow concentration-dependent mode. The rate of the slow mode decreases with increasing concentration.

With two statistically independent modes, we have

$$g^{(1)}(t) = P_1 e^{-\Gamma_1 t} + (1 - P_1)e^{-\Gamma_2 t} \quad (4)$$

where Γ_1 and Γ_2 are the relaxation rates of the fast and slow modes, respectively, and P_1 and $1 - P_1$ are their relative weights. Shown in Figure 6 as solid lines are best fits to the data using eqs 3 and 4. Both Γ_1 and Γ_2 scale as q^2, as illustrated by the inset of Figure 6. This indicates that they both correspond to translational diffusion, and we have

$$\Gamma_i = D_i q^2 \quad (5)$$

where D_i is the diffusion coefficient. The concentration dependence of the two diffusion coefficients is presented in Figure 7, together with the variation of P_1. D_1 is essentially concentration independent, while D_2 decreases by order of magnitude within the measured concentration interval.
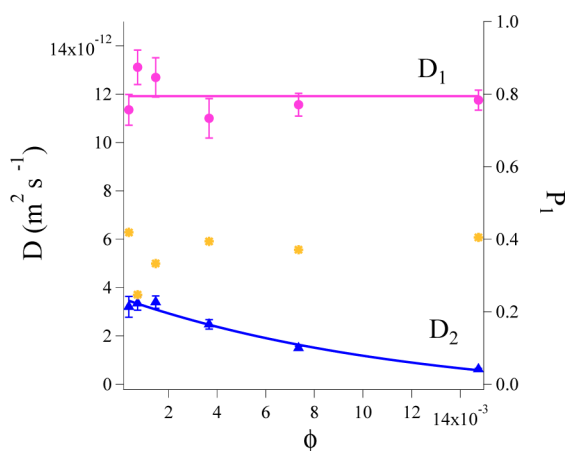

Figure 7. Concentration dependence of the two diffusion modes $D_1 = D_\parallel$ (pink circles) and $D_2 = D_\perp$ (blue triangles). Also shown is the variation with concentration of the relative weight, P_1, of the fast mode (yellow asterisks).

We interpret the two diffusion modes as corresponding to diffusion in the parallel and perpendicular directions, with diffusion coefficients $D_\parallel$ and $D_\perp$, respectively. At infinite dilution they are given by[31,32]

$$D_\parallel = \frac{k_B T}{2\pi \eta_0 L}(\delta - \gamma_\parallel) \quad (6a)$$

and

$$D_\perp = \frac{k_B T}{4\pi \eta_0 L}(\delta - \gamma_\perp) \quad (6b)$$

Here η_0 is the solvent viscosity, L is the rod length, k_B is Boltzmann's constant, T is the absolute temperature, and δ, $\gamma_\parallel$, and $\gamma_\perp$ are defined as

$$\delta = \ln\left(\frac{2L}{d}\right) \quad (7a)$$

$$\gamma_\parallel = 1.27 - 7.4\left(\frac{1}{\delta} - 0.34\right)^2 \quad (7b)$$

$$\gamma_\perp = 0.19 - 4.2\left(\frac{1}{\delta} - 0.39\right)^2 \quad (7c)$$

Rodlike particles also have a third diffusion mode, rotation, that contributes to the concentration fluctuations. However, observing this mode requires $qL > 1$, and the q^2 scaling of the observed relaxation rates indicates that we do not see any influence of rotation here.

The diffusion anisotropy $D_\parallel/D_\perp$ increases rapidly with the concentration. While $D_\parallel$ is essentially concentration independent, the perpendicular diffusion experiences strong excluded volume obstruction effects. From eqs 6a, 6b, 7a, 7b, and 7c, and setting $d = 2(ab)^{1/2}$ for the effective diameter, we can calculate a rod length from the concentration-independent $D_\parallel \approx 1.2 \times 10^{-11}$ m^2 s^{-1}. Using 1.13 mPa s for the water (D_2O) viscosity, we obtain $L = 160$ nm. The samples become very viscous at the higher concentrations, which is consistent with the strong decrease of $D_\perp$. The overlap concentration can be estimated as $\phi^* \approx \pi ab/L^2 \approx 0.001$. As seen in Figure 6, this is approximately where the slow mode begins to show a concentration dependence. With increasing concentration, the solutions approach an arrested gel state where $D_\perp$ effectively is expected to become zero. However, for $\phi > 0.02$, the samples were optically birefringent, indicating that they form a nematic phase. At infinite dilution, theory predicts $D_\parallel/D_\perp \approx 2$, but we observe rather a ratio of 3 at the lowest concentrations. The reason may be that we are not sufficiently far below ϕ^*. We also do not include polydispersity in the analysis. A few concentrations of A_8K were also studied by DLS, and similar results were obtained. L was found to be similar to that of $A_{10}K$, but slightly longer, ~ 200 nm.

3.4. Equilibrium vs Nonequilibrium Self-Assembly. A striking conclusion from the DLS experiments discussed above is that the rod length is independent of the concentration. All the $A_{10}K$ samples were prepared by dilution from the very same stock solution, $\phi = 0.036$. The most reasonable explanation is that the observed length, $L = 160$ nm, is the result of the preparation of the $\phi = 0.036$ stock solution and that there is no relaxation of this parameter when the sample is diluted. This is in contrast to what is expected for an equilibrium self-assembly system of rodlike particles. Linear equilibrium aggregation is isodesmic[24,25] and characterized by an exponential size distribution, $\exp\{-L/\langle L\rangle\}$, where the average length varies with the concentration as $\langle L\rangle \approx \phi^{1/2}$. The constant value of L here indicates the aggregates are not equilibrium states, such as surfactant micelles, but rather nonequilibrium "nanoparticles" precipitated from supersaturated solutions.

Being nonequilibrium states, one expects, for example, that their length L depends on how the sample was prepared, i.e., on the sample history. To investigate this, we prepared two $\phi \approx 0.0087$ samples using two different preparation protocols. In the first protocol the sample was prepared by direct solubilization of the freeze-dried powder. We refer to this protocol as "direct preparation", DP. In the second protocol, a $\phi \approx 0.036$ sample was first prepared that then was diluted to $\phi \approx 0.0087$. We refer to this protocol as "dilution", DIL. The samples were then studied as a function of time, for a period of

over three months, using light scattering. Two individual samples were prepared according to DP and three according to DIL. The samples DIL I, DIL II, and DIL III were prepared from the $\phi \approx 0.036$ stock solution 2, 4, and 13 days, respectively, after it had been prepared.

SLS experiments were performed at different scattering angles from 30° to 130°. The data were analyzed within the Guinier approximation

$$I(q) = I(0) \exp\{-R_g{}^2 q^2/3\} \qquad (8)$$

to obtain $I(0)$, the extrapolated intensity at $q = 0$, and the radius of gyration, R_g. From R_g the rod lengths were then calculated using the thin rod approximation $L = 12^{1/2}R_g$. The scattered intensity in each experiment was normalized by the primary beam intensity. The variations with time of $I(0)$ and L are presented in parts a and b, respectively, of Figure 8. At constant
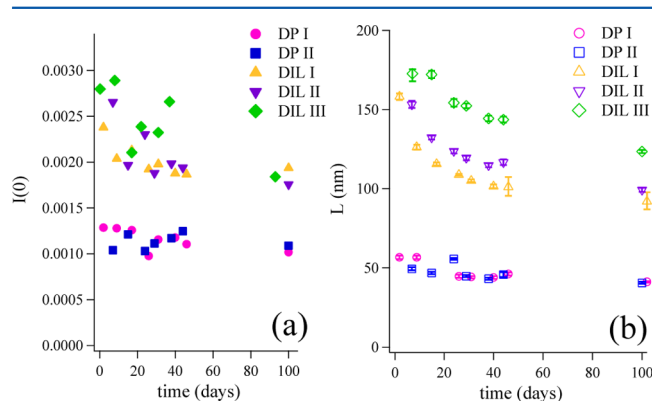

Figure 8. Variation of $I(0)$ (a) and L (b) with time for different sample preparation protocols (see the text). L was calculated from the radius of gyration.

ϕ and cross-section dimension, and assuming $S(0)$ to be independent of L (which is a reasonable approximation for $\phi > \phi^*$), we have $I(0) \approx L$, which is also approximately obtained experimentally.

The two protocols clearly result in different particle sizes, however with some reproducibility within each protocol. The average L is larger in the samples diluted from a more concentrated stock solution. Using SAXS, we confirmed that the particle cross-sections are the same in the two protocols. In the diluted samples the particle lengths decrease from ca. 150 to 100 nm during the first two months, but then seem to level off. The reason for this initial decrease is not clear. After three months the particles in the DIL samples are approximately 2 times longer than those in the DP samples.

It would be a coincidence if one of the two preparation methods produced an equilibrium state. Most likely, neither of them did. The question of thermodynamic equilibrium is important. Many applications require long-term stability. Also, for the fundamental understanding of peptide self-assembly, it is important to know whether observed structures correspond to a free energy minimum or are only kinetically stable. We can distinguish between equilibrium and nonequilibrium self-assembly. Micelle formation, with surfactants, is an example of equilibrium self-assembly where the micellar aggregates are characterized by an equilibrium size distribution. On the other hand, precipitation from a supersaturated solution, often by nucleation and growth, results in particles, e.g., nanoparticles, that are not true equilibrium states. This precipitation involves

a phase transition and a two-phase equilibrium with a macroscopic dense, often crystalline, phase coexisting with a dilute solution. Micelle formation does not involve a phase transition. Here self-assembly occurs within a single phase. These are fundamental questions that we now should apply to peptide self-assembly.

The self-assembly behavior observed in the $A_{10}K$ system indicates that it corresponds to nonequilibrium self-assembly and the precipitation of a solid phase. The fact that the peptide aggregates show crystalline order, as seen from the WAXS pattern in Figure 5b, also supports the notion of non-equilibrium. Equilibrium micelles are always in a fluid (amorphous) state and only form with molten chains above the so-called Krafft temperature. We conclude that the $A_{10}K$ aggregates resemble nanoparticles rather than micelles.

The dry pure peptide is obtained as a white solid that has been freeze dried. Because the solid spontaneously dissolves in water, resulting in submicrometer-sized aggregates, one may be tempted to interpret this as equilibrium self-assembly, i.e., micelle formation. However, the freeze-dried solid is amorphous, showing only a broad hump in WAXS data that are not shown. An amorphous state is generally less stable compared to a crystalline state. Thus, the amorphous state has a higher solubility in a solvent, which can be orders of magnitude higher, than the crystalline state. This means that, at the amorphous solubility, the solution can be significantly super-saturated with respect to the crystalline state and crystalline particles may nucleate.[33]

Finally, we note that the $A_{10}K$ particles showed no signs of Ostwald ripening, which is a general coarsening process for nonequilibrium particles driven by the interfacial energy. This may be explained by the fact that the particles are rodlike. Rodlike particles can generally be described as having an end energy, independent of their length, with the total energy then being simply proportional to the number of particles. Since moving a molecule from one particle to another then leaves the total energy unchanged, there is no net coarsening, only random exchange.

The aggregation of A_8K is very similar to that of $A_{10}K$, and it is hence reasonable to assume that the A_8K self-assembly is also in nonequilibrium. The situation appears to be somewhat different for A_6K. This peptide forms very long hollow nanotubes in water. Because of the large aspect ratio, the tubes order into a nematic (N) or hexagonal (H) phase. With a further increase of the concentration, there appears to be a first-order phase transition to a lamellar phase (L).[13] The nematic phase behaves as an equilibrium phase. The nanotubes can be recrystallized by a temperature cycle.[15] This together with the observation of a two-phase region, H + L, obeying the lever rule, implies thermodynamic equilibrium.

Peptides are reported to self-assemble into various structures such as rods or fibrils, tapes, ribbons, or hollow nanotubes. It is beyond the scope of the present paper to discuss the equilibrium state in every case. We stress, however, that the issue of equilibrium is important for general understanding and for many applications.

4. SUMMARY AND CONCLUDING REMARKS

We compare the aqueous self-assembly within the homologous peptide series A_nK. The solubility decreases approximately by an order of magnitude for every additional alanine residue. This dependence is quantitatively similar to how the solubilities of

linear alkanes, alcohols, etc., or the aqueous cmc's of surfactants, depend on the number of methylene groups.[25]

A_4K has a very high water solubility, and no aggregation was observed except for precipitation in supersaturated solutions. A_6K was studied previously and shows a striking self-assembly into hollow nanotubes, 52 nm in radius, followed by a lamellar phase at higher concentrations.[13] In the hollow A_6K nanotubes, the thin tube wall consists of a monolayer of A_6K molecules. A_8K and $A_{10}K$, on the other hand, self-assemble into thinner rodlike aggregates having a similar ellipselike cross-section. These rods are homogeneous and thus more compact. The more compact aggregates formed by A_8K and $A_{10}K$ are likely a consequence of the increased hydrophobicity. It was demonstrated that the lengths of these aggregates depend on the sample preparation protocol and hence that they correspond to nonequilibrium self-assembly. Our conclusion is that the equilibrium state here corresponds to a two-phase region, where hydrated crystalline peptide coexists with a dilute solution.

Our conclusions regarding the equilibrium phase behavior of the four studied peptides are summarized in Figure 9. Here it is assumed that the equilibrium pure (hydrated) compound is in the crystalline phase, X. This remains to be confirmed.
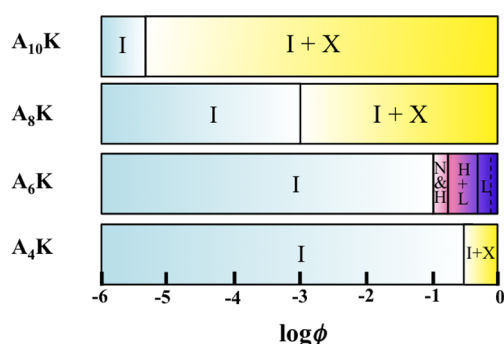

Figure 9. Tentative equilibrium phase diagrams of water−A_nK peptide systems at room temperature with n = 4, 6, 8, and 10. I denotes an isotropic liquid phase, X denotes a crystalline peptide phase, N and H are nematic and hexagonal phases of peptide nanotubes, and L denotes a peptide lamellar phase. ϕ is the peptide volume fraction. The particularly rich phase diagram of the water−A_6K system was studied previously.[13]

AUTHOR INFORMATION

Corresponding Author
*E-mail: ulf.olsson@fkem1.lu.se.

Notes
The authors declare no competing financial interest.

REFERENCES

(1) *Self-Assembled Peptide Nanostructures: Advances and Applications in Nanobiotechnology*; Castillo-León, J., Sasso, L., Svendsen, W. E., Eds.; CRC Press: Boca Raton, FL, 2012.

(2) Gazit, E. Self-Assembled Peptide Nanostructures: The Design of Molecular Building Blocks and Their Technological Utilization. *Chem. Soc. Rev.* **2007**, *36*, 1263−1269.

(3) Valery, C.; Azner, F.; Paternostre, M. Peptide Nanotubes: Molecular Organizations, Self-Assembly Mechanisms and Applications. *Soft Matter* **2011**, *7*, 9583−9594.

(4) Bowerman, C. J.; Nilsson, B. L. Review Self-Assembly of Amphipathic β-Sheet Peptides: Insights and Applications. *Biopolymers* **2012**, *98*, 169−184.

(5) Caughey, B.; Lansbury, P. T. Protofibrils, Pores, Fibrils and Neurodegeneration: Separating the Responsible Protein Aggregates from the Innocent Bystanders. *Annu. Rev. Neurosci.* **2003**, *26*, 267.

(6) Ulijn, R. V.; Woolfson, D. N. Peptide and Protein Based Materials in 2010: From Design and Structure to Function and Application. *Chem. Soc. Rev.* **2010**, *39*, 3349−3350.

(7) Matson, J. B.; Zha, R. H.; Stupp, S. I. *Curr. Opin. Solid State Mater. Sci.* **2011**, *15*, 225−235.

(8) Hosseinkhani, H.; Hong, P.-D.; Yu, D.-S. Self-Assembly of Proteins and Peptides for Regenerative Medicine. *Chem. Rev.* **2013**, *113*, 4837.

(9) Vlieghe, P.; Lisowski, V.; Martinez, J.; Khrestchatisky, M. Synthetic Therapeutic Peptides: Science and Market. *Drug Discovery Today* **2010**, *15*, 40−56.

(10) Merrifield, R. B. Solid State Synthesis. I. The Synthesis of a Tetrapeptide. *J. Am. Chem. Soc.* **1963**, *85*, 2149−2154.

(11) *Peptide Synthesis and Applications*; Howl, J., Ed.; Humana Press: Totowa, NJ, 2005.

(12) Bucak, S.; Cenker, C.; Nasir, I.; Olsson, U.; Zackrisson, M. Peptide Nanotube Nematic Phase. *Langmuir* **2009**, *25*, 4262−4265.

(13) Cenker, C. C.; Bucak, S.; Olsson, U. Nanotubes and Bilayers in a Model Peptide System. *Soft Matter* **2011**, *7*, 4868−4875.

(14) Castelletto, V.; Nutt, D. R.; Hamley, I. W.; Bucak, S.; Cenker, C.; Olsson, U. Structure of Single Walled Peptide Nanotubes: *In Situ* Flow Aligning X-ray Diffraction. *Chem. Commun.* **2010**, *46*, 6270−6272.

(15) Cenker, C. C.; Bomans, P. H. H.; Friedrich, H.; Dedeoglu, B.; Aviyente, V.; Olsson, U.; Sommerdijk, N. A. J. M.; Bucak, S. Peptide Nanotube Formation: A Crystal Growth Process. *Soft Matter* **2012**, *8*, 7463−7470.

(16) Vauthey, S.; Santoso, S.; Gong, H.; Watson, N.; Zhang, S. Molecular Self-Assembly of Surfactant-like Peptides To Form Nanotubes and Nanovesicles. *Proc. Natl. Acad. Sci. U.S.A.* **2002**, *99*, 5355−5360.

(17) Maltzahn, G.; Vauthey, S.; Santoso, S.; Zhang, S. Positively Charged Surfactant-like Peptides Self-Assemble into Nanostructures. *Langmuir* **2003**, *19*, 4332−4337.

(18) Wang, J.; Han, S.; Meng, G.; Xu, H.; Xia, D.; Zhao, X.; Schweins, R.; Lu, J. R. Dynamic Self-Assembly of Surfactant-like Peptides A_6K and A_9K. *Soft Matter* **2009**, *5*, 3870−3878.

(19) Qiu, F.; Chen, Y.; Zhao, X. Comparative Studies on the Self-Assembling Behaviors of Cationic and Catanionic Surfactant-like Peptides. *J. Colloid Interface Sci.* **2009**, *336*, 477−484.

(20) Knaapila, M. S.; Svensson, C.; Barauskas, J.; Zackrisson, M.; Nielsen, S. S.; Toft, K. N.; Vestergaard, B.; Arleth, L.; Olsson, U.; Pedersen, J. S.; Cerenius, Y. *J. Synchrotron Radiat.* **2009**, 498−504.

(21) Bellare, J. R.; Davis, H. T.; Scriven, L. E.; Talmon, Y. *J. Electron Microsc. Technol.* **1988**, *10*, 87−111.

(22) Urban, C.; Schurtenberger, P. *J. Colloid Interface Sci.* **1998**, *207*, 150−158.

(23) Block, I.; Scheffold, F. *Rev. Sci. Instrum.* **2010**, *81*, 123107.

(24) Evans, D. F.; Wennerström, H. *The Colloidal Domain. Where Physics, Chemistry, Biology and Technology Meet*, 2nd ed.; Wiley-VCH: New York, 1999.

(25) Israelachvili, J. N. *Intermolecular and Surface Forces*, 3rd ed.; Academic Press: Waltham, MA, 2011.

(26) Spalla, O. General Theorems in Small-Angle Scattering. In *Neutrons, X-rays and Light: Scattering Methods Applied to Soft Condensed Matter*; Lindner, P., Zemb, T., Eds.; North Holland, Elsevier: Amsterdam, 2002; pp 49−71.

(27) Pedersen, J. S. Modelling of Small-Angle Scattering Data from Colloids and Polymers. In *Neutrons, X-rays and Light: Scattering Methods Applied to Soft Condensed Matter*; Lindner, P., Zemb, T., Eds.; North Holland, Elsevier: Amsterdam, 2002; pp 391−420.

(28) Asakura, T.; Okonogi, M.; Horiguchi, K.; Aoki, A.; Saito, H.; Knight, P.; Williamson, M. P. Two Different Packing Arrangements of Antiparallel Polyalanine. *Angew. Chem., Int. Ed.* **2012**, *51*, 1212−1215.

(29) Serpell, L. C. Alzheimer's Amyloid Fibrils: Structure and Assembly. *Biochim. Biophys. Acta, Mol. Basis Dis.* **2000**, *1502*, 16−30.

(30) Pusey, P. Dynamic Light Scattering. In *Neutrons, X-rays and Light: Scattering Methods Applied to Soft Condensed Matter*; Lindner, P., Zemb, T., Eds.; North Holland, Elsevier: Amsterdam, 2002; pp 203−220.

(31) Broersma, S. Viscous Force Constant for a Closed Cylinder. *J. Chem. Phys.* **1960**, *32*, 1632−1635.

(32) Zero, K. M.; Pecora, R. Rotational and Translational Diffusion in Semidilute Solutions of Rigid-Rod Macromolecules. *Macromolecules* **1982**, *15*, 87−93.

(33) Lindfors, L.; Skantze, P.; Skantze, U.; Westergren, J.; Olsson, U. Amorphous Drug Nanosuspensions. 3. Particle Dissolution and Crystal Growth. *Langmuir* **2007**, *23*, 9866−9874.